High Power Laser Science and Engineering, (2024), Vol. 12, e28, 7 pages.
doi:10.1017/hpl.2024.7

HIGH POWER LASER SCIENCE AND ENGINEERING

RESEARCH ARTICLE

Generation of polarized electron beams through self-injection in the interaction of a laser with a pre-polarized plasma

L. R. Yin[1], X. F. Li[2], Y. J. Gu[3], N. Cao[4], Q. Kong[1], M. Büscher[5,6], S. M. Weng[7,8], M. Chen[7,8], and Z. M. Sheng[7,8,9]

[1] *Key Laboratory of Nuclear Physics and Ion-beam Application (MoE), Institute of Modern Physics, Department of Nuclear Science and Technology, Fudan University, Shanghai, China*

[2] *State Key Laboratory of High Field Laser Physics, Shanghai Institute of Optics and Fine Mechanics, Chinese Academy of Sciences, Shanghai, China*

[3] *SANKEN (Institute of Scientific and Industrial Research), Osaka University, Osaka, Japan*

[4] *Sichuan Research Institute, Shanghai Jiao Tong University, Chengdu, China*

[5] *Peter Grünberg Institut (PGI-6), Forschungszentrum Jülich, Jülich, Germany*

[6] *Institut für Laser- und Plasmaphysik, Heinrich-Heine-Universität Düsseldorf, Düsseldorf, Germany*

[7] *Key Laboratory for Laser Plasmas (MoE), School of Physics and Astronomy, Shanghai Jiao Tong University, Shanghai, China*

[8] *Collaborative Innovation Center of IFSA, Shanghai Jiao Tong University, Shanghai, China*

[9] *Tsung-Dao Lee Institute, Shanghai Jiao Tong University, Shanghai, China*

(Received 16 November 2023; revised 12 January 2024; accepted 6 February 2024)

Abstract

Polarized electron beam production via laser wakefield acceleration in pre-polarized plasma is investigated by particle-in-cell simulations. The evolution of the electron beam polarization is studied based on the Thomas–Bargmann–Michel–Telegdi equation for the transverse and longitudinal self-injection, and the depolarization process is found to be influenced by the injection schemes. In the case of transverse self-injection, as found typically in the bubble regime, the spin precession of the accelerated electrons is mainly influenced by the wakefield. However, in the case of longitudinal injection in the quasi-1D regime (for example, F. Y. Li *et al*., Phys. Rev. Lett. 110, 135002 (2013)), the direction of electron spin oscillates in the laser field. Since the electrons move around the laser axis, the net influence of the laser field is nearly zero and the contribution of the wakefield can be ignored. Finally, an ultra-short electron beam with polarization of 99% can be obtained using longitudinal self-injection.

Keywords: laser wakefield acceleration; longitudinal self-injection; particle-in-cell simulation; polarized electron beam

1. Introduction

As an advanced accelerator method, laser wakefield accelerators (LWFAs)[1,2] have been developing steadily both theoretically and experimentally in recent decades[3–13] owing to rapidly advancing laser technology, especially chirped-pulse amplification[14]. A variety of mechanisms have been proposed to control the electron beams properties, such as energy spectra[3–7], controllability[8], stability[9,10], beam emittance[11,12] and beam energy[13], which are comparable with those from conventional particle accelerators. Many efforts have been made with controllable injection mechanisms to improve the electron beam quality, such as density-transition injection[15,16], ionization-induced injection[17] or colliding-pulse injection[18]. However, the control of electron beam polarization has not been investigated thoroughly.

Spin-polarized electron beams have been widely used in material science[19], particle and nuclear physics[20–23].

Correspondence to: X. F. Li, State Key Laboratory of High Field Laser Physics, Shanghai Institute of Optics and Fine Mechanics, Chinese Academy of Sciences, Shanghai 201800, China. Email: xiaofengli@siom.ac.cn; Q. Kong, Key Laboratory of Nuclear Physics and Ion-beam Application (MoE), Institute of Modern Physics, Department of Nuclear Science and Technology, Fudan University, Shanghai 200433, China. Email: qkong@fudan.edu.cn

Such beams are generally produced by radiative polarization due to the Sokolov–Ternov effect in conventional accelerators[24,25], that is, storage rings, which takes around a few hours in polarization build-up. In contrast, the acceleration process can be accomplished within a few picoseconds in a plasma accelerator. In 2017, a pre-polarized gas plasma was produced through laser-induced photo-dissociation in an experiment[26]. Later, Wen *et al.*[27] proposed to generate high-current polarized electron beams with 90.6% spin polarization through an LWFA based on the density-transition injection mechanism. The study of Nie *et al.*[28,29] showed that an electron beam with up to approximately 56% polarization could be obtained using the ionization-induced injection mechanism. More recently, the effect of bubble geometry on the polarization of self-injection electrons has been studied. It was found that the deviation from a perfect spherical symmetry severely degrades the polarization of electron beams during the transverse injection[30]. Recently, Gong *et al.*[31,32] proposed that the colliding-pulse injection scheme enables the production of quasi-monoenergetic electron beams in excess of 80% polarization and tens of pC charge with commercial 10 TW laser systems in a pre-polarized plasma. Furthermore, Sun *et al.*[33] proposed to generate attosecond electron bunches with polarization of approximately 90% through using a radially polarized laser interacted with a pre-polarized plasma. Moreover, energetic spin-polarization electron beams can also be produced by a vortex Laguerre–Gaussian laser[34] or beam-driven wakefield acceleration[35].

While these injection mechanisms have been investigated to control the polarization on LWFA electron beams[27–33], a self-injection mechanism with relatively simple setup still needs to be analyzed thoroughly. There are two self-injection schemes, transverse and longitudinal, as demonstrated in Ref. [36]. The transverse injection mainly happens in the 3D nonlinear bubble regime. The accelerated electrons initially stay away from the laser axis, move in the bubble sheath, arrive at the tail of bubble and are injected in wakefield[36–40]. However, the trajectories of the accelerated electrons in the longitudinal injection scheme are different, which mainly takes place in the quasi-1D regime of the wakefield[41]. The electrons are initially located at the front of the laser pulse slip backward along the laser axis after interacting with the laser. Once reaching the tail of wakefield, the electrons are injected and finally accelerated by the wakefield[41,42].

Previous studies[27–33] have shown that the properties of the electron beams depend on the electron injection mechanism. The electron polarization mainly changes during the injection process. In this paper, we study the polarization of the electron beam for the longitudinal injection scheme in a fully pre-polarized plasma with an up-ramp-plateau density profile. The longitudinal scheme is found to be more beneficial in generating high-spin polarization electron beams as compared to the transverse case. Our work is divided into three sections. Section 2 introduces the simulation setup with a brief description of the longitudinal injection scheme. In Section 3, we present numerical results and a discussion. The conclusions can be found in Section 4.

2. Simulation method

In this study, 2D particle-in-cell (PIC) simulations were performed with a modified version of the EPOCH code[43], which includes the spin evolution module based on the Thomas–Bargmann–Michel–Telegdi (TBMT)[25,44] equation via the Boris pusher method[45]. The electron spin is regarded as a quasi-classical quantity with a vector $\boldsymbol{s}$, which has an absolute value of 1 and a direction calculated from the TBMT equation $\mathrm{d}\boldsymbol{s}/\mathrm{d}t = \boldsymbol{\Omega} \times \boldsymbol{s}$ with the following:

$$\boldsymbol{\Omega} = \frac{e}{m_\mathrm{e}}\left[\left(a_\mathrm{e}+\frac{1}{\gamma}\right)\boldsymbol{B} - \frac{a_\mathrm{e}\gamma}{\gamma+1}\boldsymbol{v}\cdot\boldsymbol{B}\frac{\boldsymbol{v}}{c^2} - \left(a_\mathrm{e}+\frac{1}{\gamma+1}\right)\frac{\boldsymbol{v}}{c^2}\times\boldsymbol{E}\right], \tag{1}$$

where m_e, e and $a_\mathrm{e} \approx 1.16 \times 10^{-3}$ are the electron mass, charge and dimensionless anomalous magnetic moment, respectively, γ is the Lorentz factor of the electron, c is the light speed in vacuum, $\boldsymbol{B}$ is the magnetic field and $\boldsymbol{E}$ is the electric field in the laboratory frame. The effects of the radiation reaction, Stern–Gerlach effect and Sokolov–Ternov effect, can be ignored during the study of LWFAs, based on the work of Thomas *et al.*[46].

In the simulation, the laser propagates in the x-direction with linear polarization and a Gaussian envelope in the y-direction:

$$E = \frac{E_0 w_0}{w(x)}\exp\left[-\frac{y^2+z^2}{w(x)^2} - \frac{(t-\tau)^2}{(0.5\tau)^2}\right]\cos(\varphi), \tag{2}$$

with the laser wavelength $\lambda = 800$ nm, the initial laser waist $w_0 = 20\lambda$, $w(x) = w_0\left[1+(x-x_0)^2/z_\mathrm{R}^2\right]^{0.5}$, $z_\mathrm{R} = \pi w_0^2/\lambda$, the pulse duration $\tau = 17$ fs and the normalized laser amplitude $a_0 = eE_0/m_\mathrm{e}\omega c = 6$, corresponding to a peak intensity of $I_0 = 7.71 \times 10^{19}$ W/cm^2. The phase is $\varphi = kx - \omega t + \phi(x) + k\left(y^2+z^2\right)/2R(x)$, where $R(x) = x\left[1+(z_\mathrm{R}/x)^2\right]$ and $\phi(x) = \arctan(x/z_\mathrm{R})$ are the radius of curvature of the beam's wavefronts and the Gouy phase at x, respectively. The simulation box is $200\lambda(x) \times 120\lambda(y)$ with resolution $\mathrm{d}x = 0.02\lambda$ and $\mathrm{d}y = 0.08\lambda$. Open boundary conditions are used in each direction and there are four pseudo-particles per cell for each particle species.

The initial longitudinal profile of the pre-polarized plasma is an up-ramp followed by a plateau with constant density $n_0 = 0.04n_\mathrm{c}$, as shown in Figure 1(a), marked with a yellow dashed line. Such a density profile makes longitudinal electron injection possible, as first introduced in Ref. [41]. Here, the length of the up-ramp transition is $L_1 = 45\lambda$

https://doi.org/10.1017/hpl.2024.7 Published online by Cambridge University Press

and the laser pulse is focused on the left-hand edge of the plasma target at $x_0 = 30\lambda$. The pre-polarized plasma could be realized by using the ultra-violet polarization method[26]. For simplicity, the initial polarization rate of the plasma is assumed as 100%, where we are interested in the evolution of the polarization during the electron self-injection scheme. The net polarization of a particle beam is defined as $P = \sqrt{\langle s_x\rangle^2 + \langle s_y\rangle^2 + \langle s_z\rangle^2}$, where s_i is the component of spin polarization in each direction and $\langle s_i\rangle$ is the corresponding average value.

3. Results and discussion

Generally, the profile of the wakefield depends on the parameters of the laser and plasma, which inevitably causes the variation of the self-injection scheme, further leading to different evolution of spin polarization during the self-injection process. When the laser spot size is larger than the plasma wavelength (Case A), the wakefield is a quasi-1D regime, as shown in Figure 1(b). At this time, the wakefield propagates in the up-ramp density. When the wakefield reaches the uniform density regime ($x = 75\lambda$), several electrons located at the tail of the wakefield ($x = 88\lambda$), can be captured and accelerated due to the breaking-wave effect, as presented in Figure 1(c). After that, owing to the effect of laser self-focusing, the laser intensity increases, the wakefield develops into a 3D nonlinear bubble regime and the electrons are accelerated continually, as revealed in Figure 1(d). On the other hand, when the laser spot size is equal to the plasma wavelength and the laser intensity a_0 is larger than 4, that is, Case B, the bubble regime can be formed directly as the laser propagates into the plasma. In order to avoid the electron at the left-hand boundary being injected into the bubble, an up-ramp density with a short length is also used, as shown in Figure 1(f). Different from the case of longitudinal injection, the bubble regime is a 3D nonlinear regime initially and the corresponding phase velocity slows down. As the bubble geometry changes following the laser evolution, several electrons can be injected into the bubble and achieve acceleration, as shown in Figure 1(g).

Not surprisingly, the distribution of the electron polarization is different in the two cases and the influence of the laser on the electron polarization cannot be ignored. In the quasi-1D regime (Case A), the values of s_x for injection electrons mostly are positive, as plotted in Figure 1(c). Meanwhile, in the bubble regime (Case B), the values of s_x about the electrons located at the sheath are negative, as revealed in Figure 1(f). For further analysis, the accelerated electrons are chosen to analyze the evolution of polarization, as marked in the green region in Figures 1(d) and 1(g), respectively. For Case A, 6056 electrons are chosen with a polarization $P = 0.99$. For Case B, there are 32,078 electrons chosen with a polarization $P = 0.18$. Moreover, as presented

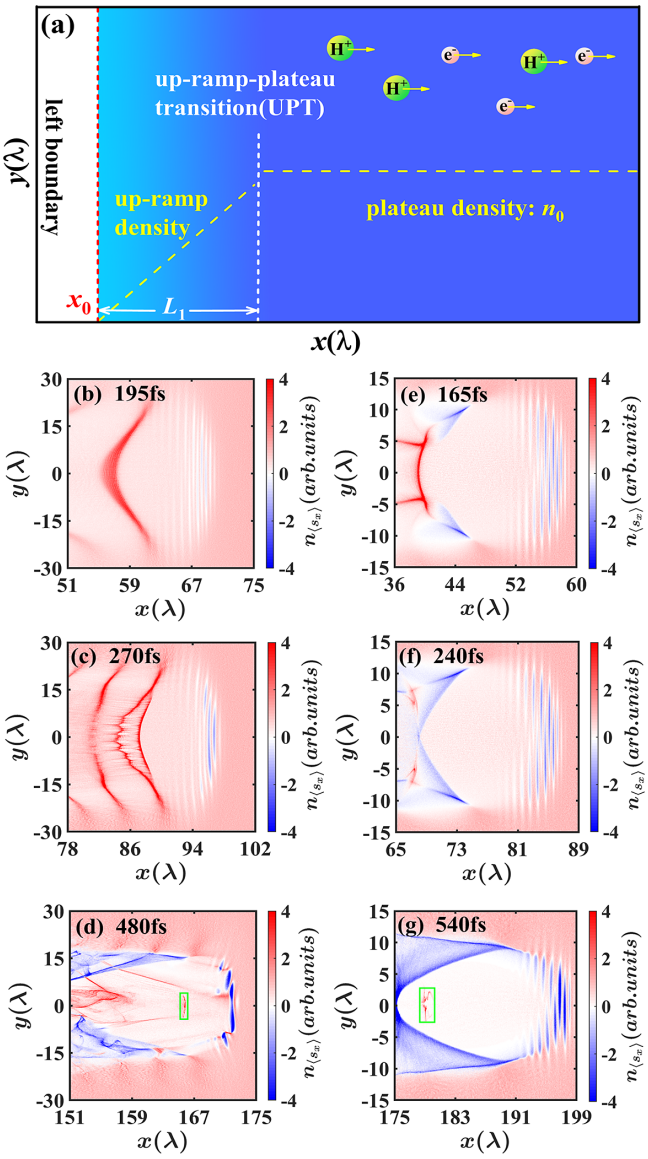

Figure 1. (a) Schematic representation of the initially pre-polarized plasma. The longitudinal profile of the electron density is marked by the yellow dashed line, including an up-ramp from 0 to n_0 with length L_1 and a plateau with n_0. The initial polarization direction is aligned along the x-direction, as denoted by the arrows. The laser is focused at the left-hand boundary of the plasma ($x_0 = 30\lambda$). For the case of longitudinal injection (Case A), (b)–(d) show the density distribution of electron longitudinal polarization $(n_{\langle s_x\rangle})$ at three different times, that is, $n_{\langle s_x\rangle}$ is the product of electron density (normalized by n_0) and the average of polarization in the x-direction ($\langle s_x\rangle$) per cell. Here, $a_0 = 6$, $\tau = 17$ fs, $w_0 = 20\lambda$, $n_0 = 0.04n_c$ and $L_1 = 45\lambda$. For the case of transverse injection (Case B), (e)–(g) present the corresponding distributions of $n_{\langle s_x\rangle}$ at different times, where $w_0 = 10\lambda$, $n_0 = 0.01n_c$, $L_1 = 10\lambda$ and the other parameters are the same as in Case A. The electrons with kinetic energy $E_k > 13$ MeV in Case A (or $E_k > 30$ MeV in Case B) are chosen as the accelerated electrons, which are marked by a green box in (d) and (g), respectively.

in Figure 1(d), another bunch of electrons ($x \simeq 150\lambda$) was injected in the wakefield owing to the nonlinear evolution of the laser pulse and bubble, which has been analyzed in the work of Kalmykov *et al.*[39,40]. The trajectories of

https://doi.org/10.1017/hpl.2024.7 Published online by Cambridge University Press

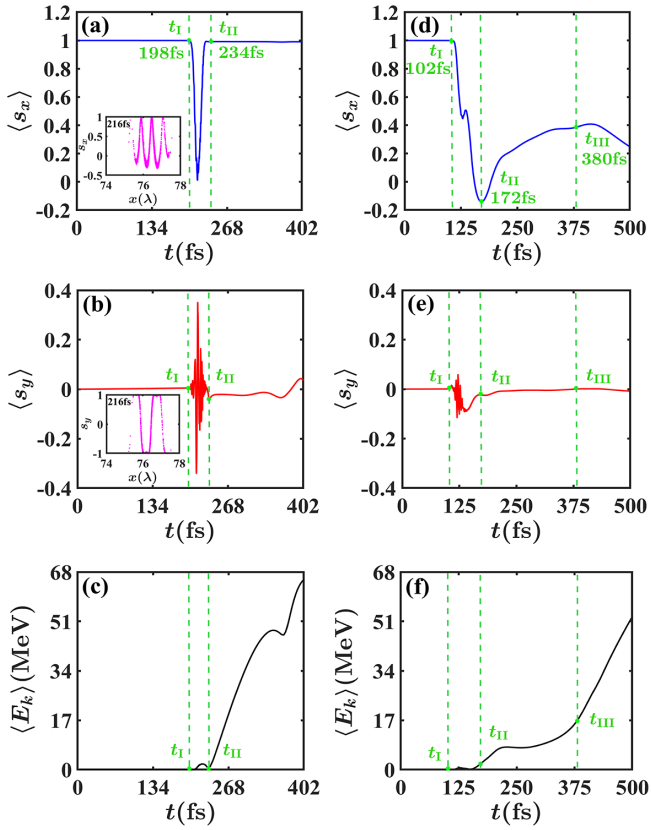

Figure 2. The history of particle properties, $\langle s_x\rangle$ (a), $\langle s_y\rangle$ (b) and the average kinetic energy $\langle E_{\rm k}\rangle$ (c) about accelerated electrons in the case of the longitudinal scheme. The distribution of s_x (or s_y) in the x-direction is shown in the insert of (a) (or (b)). (d)–(f) The corresponding quantities in the case of the transverse scheme. The accelerated electrons are marked in the Figures 1(d) and 1(g), respectively.

these electrons are similar to those in the case of transverse injection (Case B). Their polarization is nearly 0.8, which is lower than that of the first bunch of electrons; this will be discussed in this paper.

The histories of $\langle s_x\rangle$, $\langle s_y\rangle$ and the average energy $\langle E_{\rm k}\rangle$ for these two cases are plotted in Figure 2. As presented in Figures 2(a)–2(c), the evolution of the polarization for the longitudinal injection can be divided into three stages. (i) Here, $t < t_{\rm I} = 198$ fs, with the electron fixed. (ii) Here, $t_{\rm I} < t < t_{\rm II} = 234$ fs, where the value of $\langle s_x\rangle$ decreases firstly and then returns nearly to the initial value during a short time, which is nearly the duration of the laser (~ 36 fs). As presented in the insert of Figure 2(a), the distribution of s_x shows that the laser can affect the electron spin directly at 216 fs. The oscillation period is nearly 0.5λ for $\langle s_x\rangle$ and 1λ for $\langle s_y\rangle$, which means that the electron spin is affected by the laser field directly. Meanwhile, the average energy increases firstly and then decreases. (iii) Here, $t > t_{\rm II}$, where the value of $\langle s_x\rangle$ does not change significantly. The value of $\langle s_y\rangle$ is nearly 0 owing to the azimuthal symmetry of the wakefield. At this stage, the electron energy increases with time, which means the electrons are continuously accelerated in the wakefield.

For the case of the transverse injection scheme (Case B), as analyzed in Ref. [30], the evolution of polarization can be divided into four stages. (i) Here, $t < t_{\rm I}$, where the electrons do not feel the wakefield. (ii) Here, $t_{\rm I} < t < t_{\rm II}$, where the electrons are located on the bubble shell. Further, $\langle s_x\rangle$ decreases and $\langle s_y\rangle$ oscillates in the laser field and stays at nearly 0 due to the azimuthal symmetry of the bubble field, as shown in Figure 2(d). (iii) Here, $t_{\rm II} < t < t_{\rm III}$, where the electrons reach the tail of the bubble and $\langle s_x\rangle$ increases, as revealed in Figure 2(d). (iv) Here, $t > t_{\rm III}$, where the electrons are captured in the bubble and their spin precession slows down.

The electron spin evolution during the transverse injection has been studied through single particle dynamics in the work of Fan *et al.*[30]. It is found that the electron spin is mainly affected by the magnetic field of the bubble during the second stage and affected by the electric field of the bubble in the third stage. In the fourth stage, the electron moves along with the laser axis, so its spin does not change obviously. For the longitudinal injection, a typical accelerated electron is also analyzed, as shown in Figure 3. The trajectory of the electron in the wakefield coordinate system between 195 and 235 fs is presented in Figure 3(a). At 195 fs, the electron is located at the head of the wakefield, and then it slips backward. When reaching the tail of the wakefield, it is captured. Although it vibrates in the transverse direction, the transverse position does not change obviously in the wakefield.

Moreover, the evolutions of s_x and s_y are plotted in Figure 3(b). Based on the TBMT equation, the electron spin precesses in the XY plane with the laser field. Its spin changes rapidly in the laser field and the s_x returns to its initial value at each cycle. The amplitude of oscillation coincides with the laser intensity, and the profile of s_x is similar to the laser duration. However, the period of oscillation increases firstly and then decreases. If we defined the spin angle $\theta = \arctan\left(s_y/s_x\right)$, the quiver of electron spin is presented more clearly in Figure 3(c). The electron spin oscillates around the x-direction in the laser field and it causes the oscillation period of s_y to be twice as that of s_x. In addition, the period of oscillation decreases with time.

In order to investigate the dynamics of the electron spin, the contribution of the electromagnetic field to the precession frequency $\boldsymbol{\Omega}$ is analyzed in detail. Equation (1) can be rewritten as $\boldsymbol{\Omega} = \boldsymbol{\Omega}_{\rm a} + \boldsymbol{\Omega}_{\rm T}$, where the following applies:

$$\boldsymbol{\Omega}_{\rm a} = a_{\rm e}\frac{e}{m_{\rm e}}\left(\boldsymbol{B} - \frac{\gamma}{\gamma+1}\boldsymbol{v}\cdot\boldsymbol{B}\frac{\boldsymbol{v}}{c^2} - \frac{\boldsymbol{v}}{c^2}\times\boldsymbol{E}\right), \tag{3}$$

and

$$\boldsymbol{\Omega}_{\rm T} = \frac{e}{m_{\rm e}}\left(\frac{1}{\gamma}\boldsymbol{B} - \frac{1}{\gamma+1}\frac{\boldsymbol{v}}{c^2}\times\boldsymbol{E}\right). \tag{4}$$

https://doi.org/10.1017/hpl.2024.7 Published online by Cambridge University Press

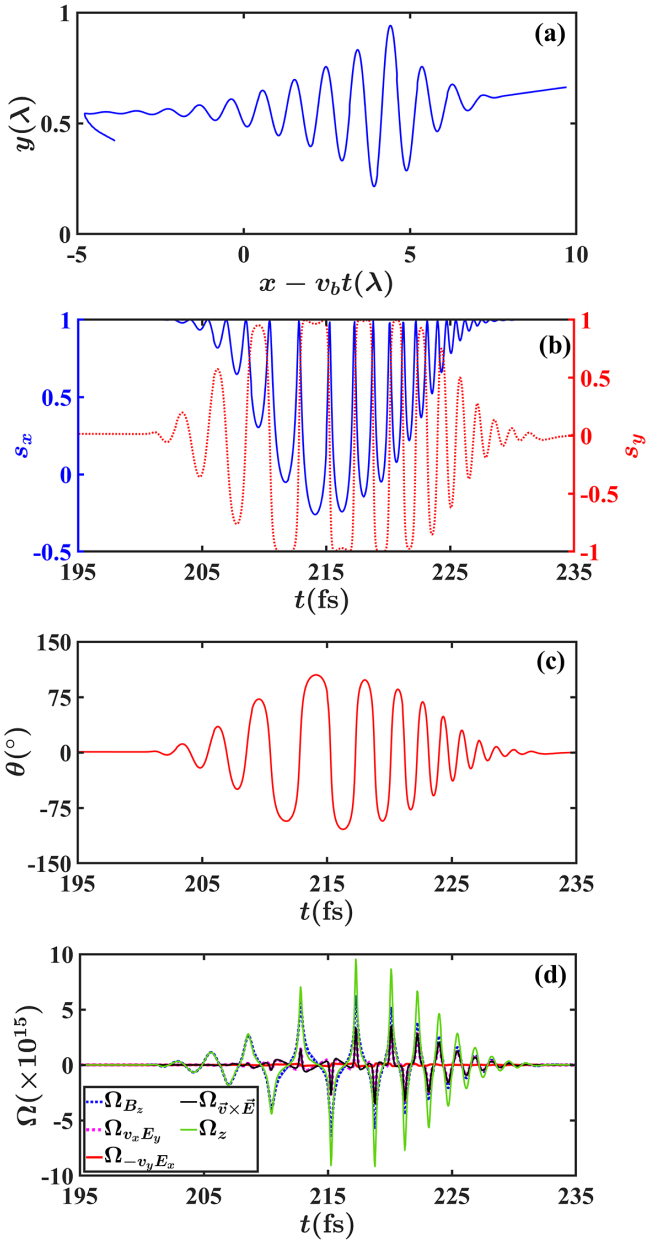

Figure 3. (a) Trajectory of a typical tracked electron for the longitudinal self-injection scheme (Case A) at the wakefield frame, where v_b is the phase velocity of the wakefield calculated using the plateau density. The electron is initially located at the front of the wakefield. (b) The history of s_x (blue solid line) and s_y (red dashed line) for the tracked electron. (c) The evolution of the spin direction $(\theta = \arctan(s_y/s_x))$ with time. (d) The evolution of $\boldsymbol{\Omega}_z$ (green solid line), the term $\boldsymbol{\Omega}_{B_z}$ (blue dashed line) and the term $\boldsymbol{\Omega}_{v_x E_y}$ (magenta dashed line) of $\boldsymbol{\Omega}_{\boldsymbol{v}\times\boldsymbol{E}}$ (black solid line) caused by $v_x E_y$, and the term $\boldsymbol{\Omega}_{-v_y E_x}$ (red solid line) of $\boldsymbol{\Omega}_{\boldsymbol{v}\times\boldsymbol{E}}$ caused by $-v_y E_x$ for the tracked electron.

Considering $a_e \approx 1.16 \times 10^{-3}$ for electrons, the value of $\boldsymbol{\Omega}_a$ is much smaller than $\boldsymbol{\Omega}_T$ at the initial stage of acceleration, that is, $a_e \ll 1/\gamma$. With the increase of electron energy, the contribution of $\boldsymbol{\Omega}_a$ gradually increases and cannot be ignored, especially when $\gamma \simeq 1/a_e \simeq 862$. As presented in Figure 2(c), the electron energy is smaller than 10 MeV during the process of injection. Therefore, the contribution of $\boldsymbol{\Omega}_a$ can be ignored and $\boldsymbol{\Omega} \simeq \boldsymbol{\Omega}_T$ can be used in the next analysis.

As shown in Figure 3(c), the electron precesses in the XY plane, which is caused by the part of $\boldsymbol{\Omega}_z$. It can be divided into three terms, $\boldsymbol{\Omega}_{B_z}$, $\boldsymbol{\Omega}_{-v_y E_x}$ and $\boldsymbol{\Omega}_{v_x E_y}$. Figure 3(d) presents the history of $\boldsymbol{\Omega}_z$, and the contributions of the three different terms have been compared. It is found that the contribution of $\boldsymbol{\Omega}_{-v_y E_x}$ can be ignored because the motion of electrons is nearly along the laser axis, where E_x is nearly zero. The contribution of $\boldsymbol{\Omega}_{v_x E_y}$ is comparable with $\boldsymbol{\Omega}_{\boldsymbol{v}\times\boldsymbol{E}}$. Following with time, the contribution of $\boldsymbol{\Omega}_{\boldsymbol{v}\times\boldsymbol{E}}$ increases firstly and then decreases, which is consistent with the evolution of electron velocity. More importantly, the net contribution of $\boldsymbol{\Omega}_z$ is nearly zero at one cycle, such that the effect of the laser field on electron spin can be ignored.

As revealed in Figure 2(a), in the third stage, the electron spin does not change obviously. The distribution of the magnetic field at 330 fs is shown in Figure 4(a). The accelerated electrons are denoted as green dots and they are located at the tail of the wakefield. The spectrum of s_x indicates that the spin does not change obviously compared with the initial value, as presented in Figure 4(b), which means that the effect of the wakefield can be ignored. Furthermore, the width of the accelerated electron beam is 0.039λ (or 103.20 as), where the full width at half maximum (FWHM) of the energy spectrum was used. The distribution of the electromagnetic field at the laser axis is presented in Figure 4(c) and the spectra of v_x and v_y are plotted in

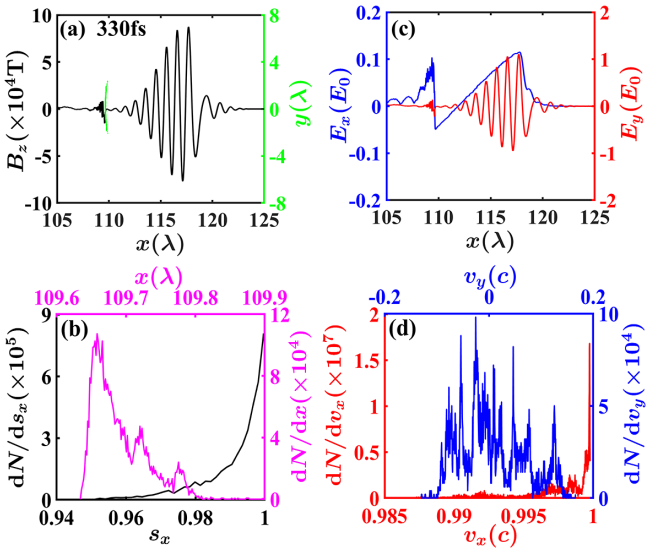

Figure 4. (a) The green dots denote the positions of the chosen accelerated electrons, which are marked in Figure 1(d). The magnetic field B_z at the laser axis is presented as a black solid line. (b) The spectra of s_x (black line) and the longitudinal position x (magenta line) for the accelerated electrons at 330 fs. (c) The profiles of E_y (red line) and E_x (blue line) at the laser axis. (d) The spectra of the longitudinal velocity v_x (red line) and transverse velocity v_y (blue line).

https://doi.org/10.1017/hpl.2024.7 Published online by Cambridge University Press

Figure 4(d). At the tail of the wakefield, B_z and E_y are nearly zero. Then their contribution to $\boldsymbol{\Omega}_z$ can be ignored. Because of the small v_y, the contribution of $\boldsymbol{\Omega}_{-v_y E_x}$ can also be ignored, which is an essential difference compared with transverse injection. In the case of longitudinal injection, due to the motion of electrons close to the laser axis, the electron spin is affected by the laser field only. Since the laser field cannot depolarize the electrons, it is advantageous to obtain a polarized electron beam with a high energy in LWFAs. Finally, a nearly 115 as electron beam with 99% polarization and average kinetic energy of 64 MeV is obtained at 400 fs.

In this work, the spin dynamics of injection electrons and the related physical mechanism have been briefly addressed based on a series of 2D simulations. Since the evolutions of the laser pulse and bubble regime are 3D nonlinear phenomena, it is necessary to use 3D simulation to analyze more accurately the characteristics of the electron beam, such as electron charge and transverse emittance[40,47].The polarization of electron beams could also be influenced by other effects, that is, beam loading and laser polarization. Besides, a plasma with 100% of the initial polarization rate was assumed since the state of pre-polarization has not been measured in the experiment. The polarization of the acceleration electron could be smaller than the result of simulation, even using the longitudinal injection mechanism. The details will be studied in our future work.

4. Summary

We have studied the generation of an electron beam, including its polarization properties in the bubble regime of an LWFA. By using a series of 2D PIC simulations, it is found that the depolarization process depends on the self-injection scheme. Compared with transverse self-injection, longitudinal self-injection is more suitable to generate an electron beam with higher polarization. The accelerated electrons move around the laser axis in the case of longitudinal injection. It causes the motion and the spin of the electrons to oscillate in the laser field, and the net influence of the laser field can be ignored. The contribution of the bubble field to the spin precession is also negligible, since the transverse electromagnetic field and the transverse velocity of the electrons are both very small. Ultimately, an attosecond electron beam with polarization of 99% is obtained in the simulation. Our work helps to generate a polarized electron beam using the longitudinal self-injection scheme in a pre-polarized plasma and guide future experiments for producing ultra-short electron beams with high polarization.

Acknowledgements

This work was supported by the National Natural Science Foundation of China (Nos. 11804348, 11775056, 11975154 and 11991074) and the Science Challenge Project (No. TZ2018005). X. F. Li was also supported by the Shanghai Pujiang Program (No. 23PJ1414600). The work of M. Büscher was carried out in the framework of the Jülich Short-Pulse Particle and Radiation Center[48] and was supported by the Accelerator Technology Helmholtz Infrastructure consortium ATHENA.

References

1. T. Tajima and J. Dawson, Phys. Rev. Lett. **43**, 267 (1979).
2. E. Esarey, C. Schroeder, and W. Leemans, Rev. Mod. Phys. **81**, 1229 (2009).
3. A. J. Gonsalves, K. Nakamura, J. Daniels, C. Benedetti, C. Pieronek, T. C. H. de Raadt, S. Steinke, J. H. Bin, S. S. Bulanov, J. van Tilborg, C. G. R. Geddes, C. B. Schroeder, C. Tóth, E. Esarey, K. Swanson, L. Fan-Chiang, G. Bagdasarov, N. Bobrova, V. Gasilov, G. Korn, P. Sasorov, and W. P. Leemans, Phys. Rev. Lett. **122**, 084801 (2019).
4. C. G. R. Geddes, C. Toth, J. van Tilborg, E. Esarey, C. B. Schroeder, D. Bruhwiler, C. Nieter, J. Cary, and W. P. Leemans, Nature **431**, 538 (2004).
5. S. P. D. Mangles, C. D. Murphy, Z. Najmudin, A. G. R. Thomas, J. L. Collier, A. E. Dangor, E. J. Divall, P. S. Foster, J. G. Gallacher, C. J. Hooker, D. A. Jaroszynski, A. J. Langley, W. B. Mori, P. A. Norreys, F. S. Tsung, R. Viskup, B. R. Walton, and K. Krushelnick, Nature **431**, 535 (2004).
6. J. Faure, Y. Glinec, A. Pukhov, S. Kiselev, S. Gordienko, E. Lefebvre, J.-P. Rousseau, F. Burgy, and V. Malka, Nature **431**, 541 (2004).
7. X. M. Wang, R. Zgadzaj, N. Fazel, Z. Y. Li, S. A. Yi, X. Zhang, W. Henderson, Y.-Y. Chang, R. Korzekwa, H.-E. Tsai, C.-H. Pai, H. Quevedo, G. Dyer, E. Gaul, M. Martinez, A. C. Bernstein, T. Borger, M. Spinks, M. Donovan, V. Khudik, G. Shvets, T. Ditmire, and M. C. Downer, Nat. Commun. **4**, 1988 (2013).
8. M. H. Cho, V. B. Pathak, H. T. Kim, and C. H. Nam, Sci. Rep. **8**, 16924 (2018).
9. J. Osterhoff, A. Popp, Z. Major, B. Marx, T. P. Rowlands-Rees, M. Fuchs, M. Geissler, R. Hörlein, B. Hidding, S. Becker, E. A. Peralta, U. Schramm, F. Grüner, D. Habs, F. Krausz, S. M. Hooker, and S. Karsch, Phys. Rev. Lett. **101**, 085002 (2008).
10. A. Buck, J. Wenz, J. Xu, K. Khrennikov, K. Schmid, M. Heigoldt, J. M. Mikhailova, M. Geissler, B. Shen, F. Krausz, S. Karsch, and L. Veisz, Phys. Rev. Lett. **110**, 185006 (2013).
11. E. Brunetti, R. P. Shanks, G. G. Manahan, M. R. Islam, B. Ersfeld, M. P. Anania, S. Cipiccia, R. C. Issac, G. Raj, G. Vieux, G. H. Welsh, S. M. Wiggins, and D. A. Jaroszynski, Phys. Rev. Lett. **105**, 215007 (2010).
12. R. Weingartner, S. Raith, A. Popp, S. Chou, J. Wenz, K. Khrennikov, M. Heigoldt, A. R. Maier, N. Kajumba, M. Fuchs, B. Zeitler, F. Krausz, S. Karsch, and F. Grüner, Phys. Rev. Spec. Top. Accel. Beams **15**, 111302 (2012).
13. W. P. Leemans, B. Nagler, A. J. Gonsalves, C. Tóth, K. Nakamura, C. G. R. Geddes, E. Esarey, C. B. Schroeder, and S. M. Hooker, Nat. Phys. **2**, 696 (2006).
14. G. Mourou and D. Umstadter, Phys. Fluids B: Plasma Phys. **4**, 2315 (1992).
15. S. Bulanov, N. Naumova, F. Pegoraro, and J. Sakai, Phys. Rev. E **58**, R5257 (1998).
16. J. Wang, M. Zeng, D. Z. Li, X. Wang, W. Lu, and J. Gao, Matter Radiat. Extremes **7**, 054001 (2022).

https://doi.org/10.1017/hpl.2024.7 Published online by Cambridge University Press

17. A. Pak, K. A. Marsh, S. F. Martins, W. Lu, W. B. Mori, and C. Joshi, Phys. Rev. Lett. **104**, 025003 (2010).
18. E. Esarey, R. Hubbard, W. Leemans, A. Ting, and P. Sprangle, Phys. Rev. Lett. **79**, 2682 (1997).
19. P. J. Schultz and K. G. Lynn, Rev. Mod. Phys. **60**, 701 (1988).
20. C. Glashausser, Annu. Rev. Nucl. Particle Sci. **29**, 33 (1979).
21. J. R. Danielson, D. H. E. Dubin, R. G. Greaves, and C. M. Surko, Rev. Mod. Phys. **87**, 247 (2015).
22. G. Moortgat-Pick, T. Abe, G. Alexander, B. Ananthanarayan, A. A. Babich, V. Bharadwaj, D. Barber, A. Bartl, A. Brachmann, S. Chen, J. Clarke, J. E. Clendenin, J. Dainton, K. Desch, M. Diehl, B. Dobos, T. Dorland, H. K. Dreiner, H. Eberl, J. Ellis, K. Flöttmann, H. Fraas, F. Franco-Sollova, F. Franke, A. Freitas, J. Goodson, J. Gray, A. Han, S. Heinemeyer, S. Hesselbach, T. Hirose, K. Hohenwarter-Sodek, A. Juste, J. Kalinowski, T. Kernreiter, O. Kittel, S. Kraml, U. Langenfeld, W. Majerotto, A. Martinez, H.-U. Martyn, A. Mikhailichenko, C. Milstene, W. Menges, N. Meyners, K. Mönig, K. Moffeit, S. Moretti, O. Nachtmann, F. Nagel, T. Nakanishi, U. Nauenberg, H. Nowak, T. Omori, P. Osland, A. A. Pankov, N. Paver, R. Pitthan, R. Pöschl, W. Porod, J. Proulx, P. Richardson, S. Riemann, S. D. Rindani, T. G. Rizzo, A. Schälicke, P. Schüler, C. Schwanenberger, D. Scott, J. Sheppard, R. K. Singh, A. Sopczak, H. Spiesberger, A. Stahl, H. Steiner, A. Wagner, A. M. Weber, G. Weiglein, G. W. Wilson, M. Woods, P. Zerwas, J. Zhang, and F. Zomer, Phys. Rep. **460**, 131 (2008).
23. V. Shiltsev and F. Zimmermann, Rev. Mod. Phys. **93**, 015006 (2021).
24. A. A. Sokolov and I. M. Ternov, Sov. Phys. J. **10**, 39 (1967).
25. S. R. Mane, Yu. M. Shatunov, and K. Yokoya, Rep. Prog. Phys. **68**, 1997 (2005).
26. D. Sofikitis, P. Glodic, G. Koumarianou, H. Jiang, L. Bougas, P. C. Samartzis, A. Andreev, and T. P. Rakitzis, Phys. Rev. Lett. **118**, 233401 (2017).
27. M. Wen, M. Tamburini, and C. H. Keitel, Phys. Rev. Lett. **122**, 214801 (2019).
28. Z. Nie, F. Li, F. Morales, S. Patchkovskii, O. Smirnova, W. An, N. Nambu, D. Matteo, K. A. Marsh, F. Tsung, W. B. Mori, and C. Joshi, Phys. Rev. Lett. **126**, 054801 (2021).
29. Z. Nie, F. Li, F. Morales, S. Patchkovskii, O. Smirnova, W. An, C. Zhang, Y. Wu, N. Nambu, D. Matteo, K. A. Marsh, F. Tsung, W. B. Mori, and C. Joshi, Phys. Rev. Res. **4**, 033015 (2022).
30. H. C. Fan, X. Y. Liu, X. F. Li, J. F. Qu, Q. Yu, Q. Kong, S. M. Weng, M. Chen, M. Büscher, P. Gibbon, S. Kawata, and Z. M. Sheng, New J. Phys. **24**, 083047 (2022).
31. Z. Gong, M. J. Quin, S. Bohlen, C. H. Keitel, K. Põder, and M. Tamburini, Matter Radiat. Extremes **8**, 064005 (2023).
32. S. Bohlen, Z. Gong, M. J. Quin, M. Tamburini, and K. Põder, Phys. Rev. Res. **5**, 033205 (2023).
33. T. Sun, Q. Zhao, F. Wan, Y. I. Salamin, and J. X. Li, Phys. Rev. Lett. **132**, 045001 (2024).
34. Y. T. Wu, L. L. Ji, X. S. Geng, Q. Yu, N. W. Wang, B. Feng, Z. Guo, W. Q. Wang, C. Y. Qin, X. Yan, L. G. Zhang, J. Thomas, A. Hützen, M. Büscher, T. P. Rakitzis, A. Pukhov, B. F. Shen, and R. X. Li, New J. Phys. **21**, 073052 (2019).
35. Y. T. Wu, L. L. Ji, X. S. Geng, Q. Yu, N. W. Wang, B. Feng, Z. Guo, W. Q. Wang, C. Y. Qin, X. Yan, L. G. Zhang, J. Thomas, A. Hützen, A. Pukhov, M. Büscher, B. F. Shen, and R. X. Li, Phys. Rev. E **100**, 043202 (2019).
36. S. Corde, C. Thaury, A. Lifschitz, G. Lambert, K. Ta Phuoc, X. Davoine, R. Lehe, D. Douillet, A. Rousse, and V. Malka, Nat. Commun. **4**, 1501 (2013).
37. S. V. Bulanov, F. Pegoraro, A. M. Pukhov, and A. S. Sakharov, Phys. Rev. Lett. **78**, 4205 (1997).
38. A. Pukhov and J. Meyer-ter-Vehn, Appl. Phys. B **74**, 355 (2002).
39. S. Kalmykov, S. A. Yi, V. Khudik, and G. Shvets, Phys. Rev. Lett. **103**, 135004 (2009).
40. S. Y. Kalmykov, A. Beck, S. A. Yi, V. N. Khudik, M. C. Downer, E. Lefebvre, B. A. Shadwick, and D. P. Umstadter, Phys. Plasmas **18**, 056704 (2011).
41. F. Y. Li, Z. M. Sheng, Y. Liu, J. Meyer-ter-Vehn, W. B. Mori, W. Lu, and J. Zhang, Phys. Rev. Lett. **110**, 135002 (2013).
42. M. K. Weikum, F. Y. Li, R. W. Assmann, Z. M. Sheng, and D. Jaroszynski, Nucl. Instrum. Methods Phys. Res. Sect. A **829**, 33 (2016).
43. T. D. Arber, K. Bennett, C. S. Brady, A. Lawrence-Douglas, M. G. Ramsay, N. J. Sircombe, P. Gillies, R. G. Evans, H. Schmitz, A. R. Bell, and C. P. Ridgers, Plasma Phys. Control. Fusion **57**, 113001 (2015).
44. L. H. Thomas, Nature **117**, 514 (1926).
45. X. F. Li, P. Gibbon, A. Hützen, M. Büscher, S. M. Weng, M. Chen, and Z. M. Sheng, Phys. Rev. E **104**, 015216 (2021).
46. J. Thomas, A. Hützen, A. Lehrach, A. Pukhov, L. Ji, Y. Wu, X. Geng, and M. Büscher, Phys. Rev. Accel. Beams **23**, 064401 (2020).
47. F. S. Tsung, W. Lu, M. Tzoufras, W. B. Mori, C. Joshi, J. M. Vieira, L. O. Silva, and R. A. Fonseca, Phys. Plasmas **13**, 056708 (2006).
48. M. Büscher, R. Adam, C. Tusche, A. Hützen, C. Wiemann, Y.-J. Chen, and C. M. Schneider, J. Large-scale Res. Facilit. **6**, A138 (2020).

https://doi.org/10.1017/hpl.2024.7 Published online by Cambridge University Press